

A Submillimeter Study of the Star-Forming Region NGC 7129

Andreea S. Font¹ and George F. Mitchell

Department of Astronomy and Physics, Saint Mary's University, Halifax, NS, B3H 3C3, Canada

Göran Sandell

National Radio Astronomy Observatory, P.O. Box 2, Green Bank, West Virginia 24944, U.S.A.

gsandell@gb.nrao.edu

Received _____; accepted _____

¹Present address: Department of Physics and Astronomy, University of Victoria, P.O Box 3055, Victoria, B.C., V8W 3P6, Canada. afont@noir.phys.uvic.ca

ABSTRACT

We present new molecular (^{13}CO $J=3-2$) and dust continuum (450 μm and 850 μm) maps of the NGC7129 star forming region. The maps include the Herbig Ae/Be star LkH α 234, the far-infrared source NGC 7129 FIRS2 and several other pre-stellar sources embedded within the molecular ridge. We also obtained C ^{18}O $J=3-2$ spectra at several positions within the mapped region. Both the continuum and ^{13}CO emissions show a similar morphology, displaying a sharp boundary towards the cavity. A new protostar (SM2) is revealed in the continuum maps, not clearly seen in any earlier data set. Also, we are able to identify the highest peak emission with the deeply embedded source IRS6, a few arcseconds away from LkH α 234. Combining these new continuum observations with previous observations of the three compact far-infrared sources in the field, we make fits to the spectral energy distributions to obtain their sizes, dust temperatures, luminosities, and masses. For nine positions where we have C ^{18}O spectra, we obtain gas masses and compare with masses derived from the continuum fluxes. The masses are found to be consistent, implying little or no CO depletion onto grains. A map of the 850 μm /450 μm spectral index, α , shows a correlation between α minima and the continuum flux peaks. The dense compact sources have dust emissivity indices, β , of 1 to 1.6, while β is typically 2.0 in the surrounding cloud. The spectral index, α , increases steeply from the center of the molecular ridge, through the PDR, to the molecular cloud boundary. Although an increase in temperature will contribute to an increase in α , the observed values require a rising β through the PDR.

Subject headings: ISM: dust, molecules – submillimeter – stars: formation, pre-main sequence – stars: individual: LkH α 234

1. Introduction

NGC 7129 is a reflection nebula seen against a molecular cloud and estimated by Shevchenko *et al.* (1989) to be at a distance of 1.25 kpc. There are many signs in this region which support the idea of triggered and possibly ongoing star formation: the association of a very young cluster formed by the B3-type stars BD +65 1637 and BD +65 1638, and the B5/7-type star LkH α 234, several embedded infrared sources (Harvey *et al.* 1984; Weintraub *et al.* 1994; Cabrit *et al.* 1997) as well as reflection nebulae and Herbig-Haro (HH) objects (Hartigan & Lada 1985; Miranda *et al.* 1994). There are also several molecular outflows in the region: one associated with an optical jet near LkH α 234 (Ray *et al.*, 1990; Edwards & Snell 1983), another bipolar outflow near the far-infrared source NGC7129 FIRS 2 and a possible one driven by the T Tauri star V350 Cep (Hartigan & Lada 1985; Goodrich 1986; Miranda *et al.* 1994).

A molecular cavity is revealed in both molecular and infrared maps (Bechis *et al.* 1978; Bertout 1987), but its origin is still unknown. The location of the two bright stars, BD +65 1637 and BD +65 1638, inside the cavity, suggests three mechanisms by which the molecular cavity could have been created: (*i*) through the advancement of a photon-dominated region (PDR) around those stars, in which the molecular gas was dissociated by their intense UV radiation, (*ii*) by an expanding shell associated with stellar mass loss, or (*iii*) by radiation pressure acting on grains, together with gas-grain drag (Bechis *et al.* 1978). The two mid-B type stars BD +65 1637 and BD +65 1638 are also the oldest in the cluster, therefore stellar mass loss may have been very effective at earlier times and the winds from those two stars may have triggered the formation of other bright stars in NGC 7129, including LkH α 234 and SVS 13. As for what mechanism is dominating at present time, the question remains open. PDR models can marginally explain the line fluxes of [OI] and [CII] emission in the region, although the C-type shock models cannot be ruled out (Lorenzetti *et al.* 1999; Giannini *et al.* 1999).

In this paper, we employ new, high resolution submillimeter observations of the molecular ridge in dust continuum emission, ^{13}CO line emission, and C^{18}O line emission. One goal of the paper is to improve our picture of the structure of the ridge and the ridge-cavity boundary. Another goal is to obtain the physical properties of the compact far-infrared sources in the ridge. A third aim is to obtain the gas/dust ratio, thus determining whether CO isotopomers are a good surrogate for molecular hydrogen, or whether CO has substantially frozen out onto dust grains. Our final goal is to search for variations in the dust opacity with position through this varied field. Our mapped region includes dense molecular gas, a photodissociation region, and a powerful outflow. We might expect processes such as grain coagulation

and mantle evaporation to have a strong spatial dependency here and for this to be reflected in spatial variations of the dust emissivity index, β .

2. Observations and data reduction

We have mapped a region several arcminutes in extent around the star LkH α 234 in the NGC7129 region, in both the ^{13}CO $J=3-2$ emission line and in submillimeter continuum emission at 450 and 850 μm . In addition, we have observed the C^{18}O $J=3-2$ emission line at nine positions in the same field.

2.1. ^{13}CO and C^{18}O observations

Observations of ^{13}CO and C^{18}O $J=3-2$ were made with the James Clerk Maxwell Telescope, on Mauna Kea, Hawaii, in August 1994 and respectively November 1997, with receiver B3i and the (Digital) Autocorrelation Spectrometer (DAS). The position switching technique was used, where the reference signal was obtained from an off-source location 10' East of LkH α 234, which was found to be free of significant CO emission. The main beam efficiency (η_{MB}) was 0.58 and the half-power beam (HPBW) was $\sim 14''$ for both ^{13}CO and C^{18}O observations.

A $7''.5 \times 7''.5$ spacing grid map was taken for the ^{13}CO $J=3-2$ (330.58 GHz) rotational transition. The map was centered on the star LkH α 234², with the coordinates $\alpha(2000) = 21^h 43^m 06^s.08$ and $\delta(2000) = 66^\circ 06' 56''.29$, and extending from $-100''$ to $+100''$ in α and from $-150''$ to $75''$ in δ offsets. The instrumental velocity resolution was 0.28 km/s. C^{18}O $J=3-2$ (329.33 GHz) spectra were taken at nine positions around the star LkH α 234 and near the molecular ridge. Figure 1 shows a superposition of the ^{13}CO integrated intensity ($\int T_B dv$) contour map on a K' image of the NGC 7129 region from Hodapp (1994). The nine C^{18}O offsets, with respect to the star LkH α 234, are shown with cross symbols and are listed in Table 2.

²The astrometric position for LkH α 234 given by Clements & Argyle (1984) is $\alpha(2000) = 21^h 43^m 06^s.802$ and $\delta(2000) = 66^\circ 06' 54''.5$.

2.2. Submillimeter continuum observations

We have obtained deep 850 μm and 450 μm -maps of LkH α 234 and the bright-rimmed cloud ridge southwest of LkH α 234 using the Submillimeter Common User Bolometer Array, SCUBA (Holland *et al.* 1999), on the 15 m James Clerk Maxwell Telescope, on Mauna Kea, Hawaii, on October 15, 1997 in Canadian service time. The weather conditions were dry and stable with an 850 μm zenith optical depth of ~ 0.19 . The two overlapping fields were obtained in jiggle-map mode with a chop-throw of 150'' in Right Ascension with a total integration time of 85 minutes/field. For a description of SCUBA and its observing modes, see Holland *et al.* (1999). Unfortunately the maps were taken without usable calibration and pointing observations and we have therefore reduced the data by determining the HPBW of the telescope from observations of Uranus from other nights in September and October with similar sky conditions. The same nights were also used to determine gain conversion factors for the 850 μm and 450 μm filters. The HPBW was found to be $\sim 15''.6 \times 13''.5$ at 850 μm and $9''.1 \times 7''.8$ at 450 μm with the beam broadened in the chop direction. The submillimeter position of LkH α 234 (Table 3), which has an accuracy of $\sim 1''$ was taken from three short-integration maps interlaced with pointing observations in SCUBA commissioning time during Spring 1997. We have not added in these maps in the final data set, because they were taken with a 120'' Azimuth chop and there is clear evidence that the array was chopping onto emission. However, if we compare the total flux density of LkH α 234 (i.e. background subtracted flux density) it agrees very well with data taken in October.

We also include a map of the H₂O maser and bipolar outflow source NGC 7129 FIRS2, which was used as a test source during SCUBA commissioning (Sandell 1997). A composite map at 850 μm , including all the three overlapping fields is shown in Figure 2.

The basic data reduction was done with SURF (Jenness & Lightfoot 1999). Even with a 150''-chop it is more than likely that we may have chopped onto some emission in both fields, but as far as we can judge, it does not appear to affect the morphology of the strong dust ridge in which LkH α 234 is embedded. We do see some negative emission west of LkH α 234, which confirms that there is emission in the off-position. It is therefore likely that emission east of the ridge is also affected, which is why the 850 and 450 μm maps appear somewhat different. To map a cloud ridge in beam switch mode is not very advisable, but at the time SCUBA was only available in jiggle map mode. We know that we have to chop into the cloud, but as long as the cloud emission is faint compared to the emission we want to map and relatively uniform, the morphology of the cloud ridge will be not affected. However, since the beam size and error lobe contribution

differs between 850 μm and 450 μm this leads to systematic errors in the integrated intensities (see Section 3.2).

The final pointing corrected and calibrated maps have an rms noise of ~ 15 mJy/beam and ~ 120 mJy/beam for 850 and 450 μm , respectively. These maps were written out as FITS files and read into MIRIAD (Sault, Teuben, & Wright 1995) for further analysis.

3. Analysis

3.1. ^{13}CO and C^{18}O Emission

A sharply bounded molecular cavity is seen in ^{13}CO $J=3-2$ emission westward of LkH α 234, most probably excavated by the B3-type star BD +65 1637. The lack of molecular emission and the ridge morphology were also noted in the CO $J=1-0$ and NH $_3$ observations (Bechis *et al.* 1978; Fuente *et al.* 1998; Güsten & Marcaide 1986). However, our high resolution (half-beam sampling with a 14'' beamsize) observations enable us to resolve the ridge structure in much more detail.

We see four ^{13}CO peaks along the ridge. One is very close to LkH α 234, two are just to the northwest of LkH α 234, and the fourth is a larger feature two arcminutes to the south. We assume that these ^{13}CO structures are physical clumps and name them NGC 7129 ^{13}CO -1, NGC 7129 ^{13}CO -2, NGC 7129 ^{13}CO -3, and NGC 7129 ^{13}CO -4. The positions of these four ^{13}CO peaks are given in Table 1.

Perhaps the most striking feature of the ^{13}CO map is the sharpness of the transition between the molecular cavity to the west and the molecular cloud to the east. ^{13}CO line strengths drop by factors of 20 or more across the boundary. The narrowness of the transition region between atomic and molecular gas has implications for the three dimensional topology of the region. There seem to be three possibilities: Firstly, the boundary region may be a sheet which happens to be perpendicular to the line-of-sight. Secondly, the molecular cavity may be a bowl which is surrounded by molecular gas. Thirdly, the molecular cloud may take the form of a rather narrow ridge which is partially surrounded by atomic gas. The first possibility is improbable, while the second should lead to a broader transition region (molecular to atomic). We favor the third picture, in which the dense portion of the molecular cloud consists of a clumpy ridge with a line-of-sight extent comparable to its extent in the plane of the sky (roughly 0.5 pc).

Another remarkable feature which can be seen in Figure 1 is the narrow filament of emission seen in the K' image. This filament is partially obscured by the ^{13}CO contours in Figure 1 and is better seen in

the original image (Hodapp 1994). It extends roughly south from LkH α 234 and then curves to the west, keeping a nearly constant surface brightness. The filament follows closely the outermost ^{13}CO contours which separate the cavity from the molecular cloud. In an unpublished observation using an IR camera on the CFHT with a circularly variable filter, Mitchell and Nadeau found this filament to be a source of strong emission in the S(1) $v=1-0$ line of H $_2$. A natural explanation for both the sharp molecular boundary and the line-emitting filament is the presence of a photodissociation region, or PDR. The H $_2$ S(1) $v=1-0$ line emission is then due to fluorescence. The PDR is very likely produced by UV radiation from the early B star BD+65 1638. We note however, that the detection of both types of emission at the same location is in contrast with predictions of steady state stationary PDR models (Hollenbach & Tielens 1997), where a more gradual succession of emission layers is expected as they move away from the UV ionization front, and with the H $_2$ $v=1-0$ transition layer being separated by about $10''$ from the molecular CO emission. On the other hand, this type of morphology may be explained in the framework of nonstationary PDR models (Bertoldi & Draine 1996), which show that the inhomogeneities in the molecular cloud surface can lead to the merging of the ionization and the dissociation front.

Because ^{13}CO is likely to have an appreciable optical depth, C ^{18}O 3–2 spectra were obtained at several positions. The positions for which we have C ^{18}O spectra are indicated by the cross symbols in Figure 1. A comparison between ^{13}CO and C ^{18}O spectra at the nine selected locations is shown in Figure 3. Positions are given as offsets from LkH α 234 in arcseconds. The line intensities are shown as antenna temperatures, T_A^* , after corrected for the losses due to the Earth atmosphere and the telescope. For all spectra only the linear baselines were removed, using the SPECX software package (Padman 1992).

Near LkH α 234, the lines are broadened due to contributions from the outflow. The offset position (52 $''$.5, 37 $''$.5) is near the peak of CO emission in the redshifted outflow lobe. Both ^{13}CO and C ^{18}O spectra are double peaked at this position. The value of the line ratio shows that C ^{18}O is optically thin. The two peaks therefore represent two real kinematic components rather than a single line suffering self absorption. The peak at -10 km s^{-1} ambient gas at this position, while the peak at -7 km s^{-1} is postshock gas.

Several line parameters have been calculated at each offset, assuming local thermodynamical equilibrium (LTE) conditions and a standard value for the abundance ratio of $N_{^{13}\text{CO}}/N_{\text{C}^{18}\text{O}} = 10$. The intensity ratio, $^{13}\text{CO}/\text{C}^{18}\text{O}$, is used to find the optical depth, assuming a common T_{ex} for the two transitions. Then, the value of T_{ex} is found from the LTE expression relating line strength (given by the radiation temperature), line optical depth τ , and the excitation temperature:

$$T_{exc} = \frac{h\nu/k}{\log[(1 - e^{-\tau})(kT_R/h\nu + 1)]}. \quad (1)$$

The results of the analysis are shown in Table 2. The optical depths τ_{13} , are ranging from 2.6 to 6.7. We find for LkH α 234 an excitation temperature of about 30 K, in agreement with previous values of 20 – 30 K obtained from lower resolution (70'') CO observations (Bechis *et al.* 1978) and with the 20 – 25 K obtained from NH₃ (40'') observations (Güsten & Marcaide 1986).

At the offset position (-22.5'', 10''), the gas has an excitation temperature of \sim 34 K, higher than the typical value for a dark core, but lower than the previous value of 63 K obtained by Mitchell and Matthews (1994) from ¹²CO and ¹³CO data. These two temperatures are easily reconciled. The 63 K value was found directly from the peak ¹²CO antenna temperature. ¹²CO will have a high optical depth, so the line is formed in the hotter outer zone of the PDR. With its lower optical depth, the ¹³CO line is probing deeper into the PDR where the temperature will be lower.

The three last entries in Table 2 represent positions increasing in distance from the cloud boundary. The excitation temperature is found to decrease with distance from the boundary, from 38 K through 31 K to 21 K. This decrease is in the sense expected as the stellar radiation is increasingly attenuated with distance into the molecular cloud. At the offset (52''5, 37''5), which is farthest from the cloud boundary, the excitation temperature of the ambient gas is lowest, just 13 K.

Since the clumps have approximately the same size as our beam and since our beam does not always include a clump of gas, it is reasonable to calculate the masses of the gas within the beam (14''). The results, including the fractional helium abundance and assuming a distance of 1.25 kpc to the source, are shown in Table 2. The clump at (0''0, 0''0), coincidental with the position of the star LkH α 234, contains 10.7 M_⊕. The masses within the beam, at two offsets which encompass the clump coincidental with the pre-stellar source LKH α 234 SM2 (offsets (-20''0, 25'') and (-22''5, 10'')) are 12.8 and 7.2 M_⊕, respectively. However, those values should be regarded as upper limits since the temperatures are probably lower, as suggested by the more optically thin NH₃ data.

We also caution that these results depend on the accuracy of the distance determination. The earliest distance estimate for NGC 7129 was reported by Racine (1968), but we use in our analysis the value of 1.25 kpc, determined by Shevchenko *et al.* (1989) on an improved photometry and spectral classification of 35 stars. However, if the PDR is associated with the Cepheus Bubble, as suggested by Ábrahám, Balázs & Kun (1999), then the distance could be as low as 500–700 pc, and of course, the derived masses and

luminosities will be significantly reduced.

The masses obtained in this analysis will be discussed, and compared to masses obtained from dust emission, in section 4 below.

3.2. Dust Emission

In order to compare the 850 and 450 μm dust emission with our molecular line observations, we need to convolve the 450 μm images to the same HPBW as the rest of the observations. However, since the JCMT telescope is far from perfect at 450 μm , we first need to remove the error beam. We have therefore constructed a model beam by fitting three gaussians to representative beam maps of Uranus. The main beam and the near error lobe was fitted with elliptical Gaussians, while the far error lobe was fitted with a circularly symmetric beam. The relative amplitude of the main beam and the near and far error lobes were found to be 0.925:0.07:0.005. The HPBW of the near error lobe was $37'' \times 26''$, with the major axis aligned in the chop direction similarly to the main beam (c.f. Section 2.2), and the far error lobe gave a HPBW $\sim 120''$. We tested deconvolving the images both with MAXEN (MIRIAD’s maximum entropy task) and CLEAN. Both worked reasonably well, but CLEAN is better in preserving flux, and was therefore adopted. We also constructed a model beam for 850 μm and ran CLEAN on the 850 μm –images as well. The deconvolved images were restored with a symmetric Gaussian to a $14''$ beam and for 450 μm we also made maps restored to a HPBW of $8''$. The 450 μm and 850 μm maps restored to $14''$ are shown in Figures 4 and 5.

Even CLEAN, however, is not ideal for recovering smooth extended emission, which could cause us to underestimate the 450 μm emission more than we do at 850 μm , since we restore the 450 μm –map from an $8''.5$ resolution to $14''$, while the resolution in the 850 μm –maps remain roughly the same. Emission in the off position will have an even more severe systematic effect. Since the error beam has a much higher amplitude at 450 μm than at 850 μm , any emission in the off position will affect the baselevel of the 450 μm –map much more than that at 850 μm . This leads us to systematically underestimate the flux densities at 450 μm . We have tested this by adding a constant flux level of 5% of the peak value at 450 μm to the “raw” 450 μm –map of LkH α 234. We then ran the baselevel corrected map through CLEAN and restored it to $14''$. When we compare flux densities in our $14''$ beam for positions more than $40''$ away from LkH α 234, we find that by adding a zero-level of 5% of the peak flux density, we increased the flux level by more than a factor of two compared to the uncorrected map. Since we can easily have an error of 5% in the

base level, this means that the flux densities for faint extended emission is uncertain by more than a factor of two. In this case the 450 μm flux densities are more than likely to be systematically underestimated.

We used two-dimensional Gaussian fits to determine the size and total flux of the two “compact” sources in the field, i.e. LkH α 234 SM1 and the protostellar source, LkH α 234 SM2, $\sim 28''$ of LkH α 234 SM1. Here our flux estimates are much more accurate, since the sources are compact and we can subtract the emission from the surrounding cloud ridge. We find LkH α 234 SM1 to be extended with a size of $\sim 5''$ (Table 3). This agrees well with earlier 800 μm and 450 μm maps (Sandell & Weintraub 1994) as well as with 1.3 mm maps by Fuente *et al.* (1998) and Henning *et al.* (1998). The source LkH α 234 SM2 is not obvious the 1.3 mm Fuente *et al.* (1998) nor in the map of Henning *et al.* (1998), but both 1.3 mm maps show an extension towards SM2 in good agreement with our SCUBA maps. By using the size derived from our SCUBA maps we derive an integrated 1.3 mm flux of 0.2 ± 0.04 Jy from the map published by Fuente *et al.* (1998). We are interested to derive the β -index (where β reflects the change in dust emissivity or, equivalently, the change in optical depth, with frequency, $\kappa \sim \tau \sim \nu^\beta$) and the total (gas + dust) mass. For this, we have fitted the 1.3 mm data point and the two SCUBA data points with a simple isothermal model (see e.g. Sandell 2000). Since both IRAS and KAO data (Bechis *et al.* 1978; Harvey, Wilking & Joy 1984; Di Francesco *et al.* 1998) employ large beam sizes that are likely to include hot dust from the surrounding reflection nebulosity as well, we have not included FIR data in our least squares fit, although we constrained our LkH α 234 SM1 model to the peak dust temperature derived by Harvey, Wilking & Joy (1984). The results of the fit are given in Table 4 and also shown in Figure 6. We have less constraints for LkH α 234 SM2, but looking at gas temperatures, either from our own CO observations or the NH $_3$ map by Güsten & Marcaide (1986) we find it to be ≤ 30 K, and in the fit we give in Table 4 we have constrained the fit to 30 K. The mass we derive for the dust disk surrounding LkH α 234 SM1 is about half that derived by Henning *et al.* (1998) after we adjust it to the same distance. The difference is largely due to the difference in adopted mass opacity for the dust.

In order to compare the mass estimates derived from our ^{13}CO and C^{18}O data, we have also derived the submillimeter flux densities corresponding to 14'' beam for the same offset positions as the ^{13}CO data. These are given in Table 5. If we ignore the differences in dust properties and dust temperature between the two embedded stars and assume that the dust is at the same temperature as the CO, we obtain unphysical low β -indeces. If we would use the baseline adjusted 450 μm data we would obtain $\beta \sim 1.7$, but since we don't know how to accurately correct for the emission in the off position we prefer to assume a β -index and only use the 850 μm map, since it we know it is much less affected by emission in the off position. We

also note that the CO temperatures are likely to be dominated by gas heated by the PDR, and the CO temperatures therefore provide an upper limit to the mass averaged gas temperatures. The dust emission, however, is optically thin and the sub-mm dust emission is therefore dominated by colder dust inside the dense cloud ridge. This gas is more accurately measured by NH₃, which shows kinetic temperatures of ~ 25 K (Güsten & Marcaide 1986) along the cloud ridge. In the second entry for each offset we therefore assume lower gas temperatures (typically smaller than the CO temperatures) the kinetic temperatures from CO as a guideline. We also subtracted out the two sources from the map in order to separate the dust cloud from the disk emission. However, in the column where we give total masses (Table 5) we have also include the contribution from LkH α 234 SM1 and LkH α 234 SM2.

3.3. NGC 7129 FIRS 2

NGC 7129 FIRS 2 was first discovered by Bechis *et al.* (1978) as a cold FIR source associated with a ¹³CO column density peak south of LkH α 234. It was found to coincide with an H₂O maser (Cesarsky *et al.* 1978; Rodríguez *et al.* 1980; Sandell & Olofsson 1981), suggesting that it is a young protostellar source, yet the source is invisible in the optical and near-IR. Additional FIR mapping by Harvey, Wilking & Joy (1984) confirmed the detection by Bechis *et al.* (1978) and detected the source at both 50 and 100 μ m, but not at 20 μ m or shorter wavelengths. Edwards & Snell (1983) found that FIRS 2 was associated with a CO outflow, which further strengthened its association with a young intermediate PMS star. Jenness, Padman & Scott (1995) included FIRS 2 in their survey of FIR cores in the vicinity of H₂O masers and reported a flux density of 5.2 Jy at 800 μ m and 30 Jy at 450 μ m. Eirúa, Palacios & Casali (1998) proposed that FIRS 2 is an intermediate mass Class 0 object, based on (sub)mm photometry at 2 mm, 1.3 mm, 1.1 mm and 800 μ m as well as from high resolution reconstructed IRAS data, i.e HIRAS. They detect FIRS 2 at 25, 60 and 100 μ m, but not at 12 μ m. They fit the SED of FIRS 2 with a standard isothermal graybody fit and find a β -index of 0.9 and a dust temperature of 35 K corresponding to a total mass of 6 M_⊙.

Our SCUBA data give a quite accurate position for FIRS 2, which agrees well with the H₂O position (uncertainty $\pm 10''$). We resolve the source with a FWHM of $\leq 3.7''$. We also see the surrounding cloud core, but because we mostly used relatively short chops ($\sim 100''$) we don't have a good measure of the dust emission of the cloud core. We supplement our data with maps and photometry made by us using UKT14 on JCMT. Our UKT14 flux densities are generally lower than those found by Jenness, Padman & Scott (1995) and Eirúa, Palacios and Casali (1998), but agree much better with the well-calibrated SCUBA data.

We find flux densities of 0.48 ± 0.10 Jy, 1.18 ± 0.03 Jy, 1.69 ± 0.05 Jy and 3.66 ± 0.22 Jy for 2 mm, 1.3 mm, 1.1 mm and $800 \mu\text{m}$, respectively. The flux densities at 2 mm and 1.3 mm are based on photometry and therefore also include a small contribution from the surrounding cloud. The 1.1 mm and $800 \mu\text{m}$ values are derived from Gaussian fits to calibrated maps, i.e. essentially the same way we treated our SCUBA data.

Our isothermal fit (Figure 6) predicts a $\beta \sim 1$ and a dust temperature of 42 K. The fit underestimates slightly the FIR data points, which is observed with a large beam size and therefore includes emission from the surrounding cloud core as well. Our estimated β -index and mass (see Table 4) agrees rather well with Eir  a, Palacios & Casali (1998) and demonstrates that FIRS 2 is a cold protostellar source with a luminosity of $\sim 400 L_{\odot}$.

4. Discussion

4.1. A Gas and Dust Comparison

The ^{13}CO emission (Figure 1) and dust emission (Figures 4 and 5) show broadly similar distributions. The molecular cavity is also a dust cavity, although the boundary appears broader in dust continuum emission than in ^{13}CO emission. The presence of a dust cavity suggests that the interior is not filled with HI, but has been substantially cleared of dust and gas. Bechis *et al.* (1978) showed that radiation pressure from older stars in the cavity is capable of doing this. In both ^{13}CO and dust, the mapped region is seen to contain two main clumps, one surrounding the star LkH α 234 and extending to the northwest, the second being about $2'$ to the south.

Although the dust and gas maps are consistent on large scales, there are significant differences in detail. The southern clump, centered on the peak NGC 7129 ^{13}CO -4, has an extension to the east with no counterpart in the continuum maps. In both gas and dust maps, the northern field is dominated by the compact source near LkH α 234. The ^{13}CO -2 peak is seen as an extension to the LkH α 234 source in the $850 \mu\text{m}$ map and as a separate source in the $450 \mu\text{m}$ map (LkH α 234 SM2 in Table 3). The peak ^{13}CO -3 is not present in the dust emission maps. The two peaks ^{13}CO -2 and ^{13}CO -3 have essentially equal intensity, so the difference in continuum emission between the two is surprising. The answer may lie in the proximity of the star SVS 13 to SM2. Radiation from SVS 13 may be responsible for maintaining the warm dust temperature of 30 K which we find for this source. We have no dust temperature for the ^{13}CO -3 peak, but

its projected distance from SVS 13 is about three times that of ^{13}CO -2, so the stellar radiation will be much more dilute.

A quantitative comparison of gas and dust is provided by the masses listed in Tables 2 and 5. All of these masses are within a 14" beam. The mass from the CO isotopomers was obtained from LTE expressions (see Section 3.1), while the mass from the 850 μm flux required values of β , T_d and a gas/dust mass ratio of 100:

$$M(M_\odot) = 1.88 \times 10^{-2} \times F \times \left(\frac{\lambda}{0.25}\right)^{\beta+3} \times [e^{\frac{14.4}{\lambda T_d}} - 1] \times d^2, \quad (2)$$

where F is the flux (in Jy) at the wavelength λ (in mm) and d is the distance to the source (in kpc). Three values for dust masses are given in Table 5, for different values of T and β . We will refer below to those found with $\beta = 2$, which is the typical value expected from theoretical grain models (Hildebrand 1983). In view of all the assumptions that must be made, we consider the mass values derived from CO and from dust to be in good agreement. In the worst cases, the difference is a factor of three. In all these cases, agreement could be improved by making defensible adjustments to the dust temperature. One of the important results of this gas-dust comparison is the absence of evidence for CO depletion in this region. Molecular depletion, by freeze-out onto grains, is a serious concern when molecular tracers are used as surrogates for H_2 . An example of a region where CO depletion occurs is the HH24-26 region in the Orion B molecular cloud (Gibb & Little 1998; Mitchell *et al.* 2000). The absence of depletion in the NGC 2179 ridge is due to the enhanced radiation field, which maintains grain temperatures above the 16 K CO freeze-out temperature.

4.2. The nature of the submillimeter sources LkH α 234 SM1 and SM2

Early studies of NGC 7129 (Bechis *et al.* 1978; Harvey, Wilking & Joy 1984) indicated that the FIR emission could be explained by dust heated by the B stars that illuminate the reflection nebulae. The FIR emission peaked on LkH α 234, which was also known to be a weak radio continuum source (Bertout & Thum 1982), associated with an H_2O maser (Cesarsky *et al.* 1978) and driving a high velocity CO outflow (Edwards & Snell 1983). The second FIR peak, FIR2 was also associated with an H_2O maser, and a high velocity CO outflow, but lacked an optical counterpart (see Section 3.3). Since LkH α 234 was associated with HH objects (Hartigan & Lada 1985), coincided with a free-free emission source at 15 and 22 GHz, with compact dust emission at 3 mm (Wilking, Mundy & Schwartz 1986) and drove a highly collimated optical

jet (Ray *et al.* 1990) this identification appeared rather secure.

However, Skinner, Brown & Steward (1993) noticed that the free-free emission was offset by $\sim 1''.7$ from the optical position of LkH α 234 if they adopted the more accurate optical position given by Herbig & Bell (1988) or $2''.2$ compared with the astrometric position of Clements & Argyle (1984). Near-IR polarimetric imaging by Weintraub, Kastner & Mahesh (1994) showed that there is a deeply embedded companion $\sim 3''$ of LkH α 234, which was invisible in total intensity maps in K band. High resolution mid-IR imaging by Cabrit *et al.* (1997) identify the embedded companion star, IRS 6, at $2''.7$ of LkH α 234 and show that it has a steeply rising spectrum so that at $17\mu\text{m}$ IRS 6 is as bright as LkH α 234. IRS 6 therefore coincides with the radio free-free emission source, with two H₂O maser spots, and with the 3 mm dust emission (Wilking, Mundy & Schwartz 1986; Sandell, unpublished data). Cabrit *et al.* (1997) show that IRS 6 illuminates an arc-shaped reflection nebula with very red colors and that it drives an H₂ jet at a position angle (p.a.) of 226° . The p.a. of the H₂-jet therefore differs from that of the optical [SII]-jet, which has a p.a. of 252° (Ray *et al.* 1990). Whether the much larger [SII] jet also originates from IRS 6 is not clear (Cabrit *et al.* 1997). Although Mitchell & Matthews (1994) report that the p.a. of the CO outflow agrees with the optical jet, this is not true if we look at the p.a. determined from the symmetry axis of the large scale red CO outflow, which is about $\sim 230^\circ$. Neither does the p.a. of the optical jet agree with the location of the two HH objects GGD 32 and HH 103 SW of LkH α 234 and IRS 6, which lie in the blue-shifted lobe of the CO outflow.

The sub-mm position for LkH α 234 SM1 determined from our $850\mu\text{m}$ map (Table 3) falls between LkH α 234 and IRS 6, but since our positional accuracy is $\sim 1''$, the emission could peak on either star. However, since the dust emission at 3 mm peaks on IRS 6, it is plausible to assume that the sub-mm emission also peaks on IRS 6. It therefore appears that it is the cold, heavily obscured IRS 6 that drives the CO outflow and is associated with the massive dust disk we see in sub-mm. This disk is orthogonal to the near-IR H₂ jet to within a few degrees. From our simple isothermal modeling (Section 3.2) we derive a luminosity of $\sim 9\,10^3\,L_\odot$, which would make IRS 6 an early B star, i.e. a young Herbig Be star still heavily enshrouded by dust. It is clear that LkH α 234 as well as BD+65°1638 and even BD+65°1637 and SVS 13 contribute to the 50 and $100\mu\text{m}$ emission, but the sub-mm emission is totally dominated by IRS 6 and the second sub-mm source LkH α 234 SM 2. We do see some dust emission in the molecular cavity, especially in the vicinity of BD+65°1638. This dust is hotter than the dust in the cloud ridge, which is also seen from the spectral index plot (Figure 7).

The sub-mm source LkH α 234 SM 2 does not have a known optical or IR counterpart. It is $\sim 12''$ to the east of SVS 13, which is not seen in the sub-mm maps (Figures 4 and 5). Neither does it coincide with the CO hotspot seen by Mitchell & Matthews (1994), which is $\sim 10''$ - $15''$ SE of the sub-mm source. SM 2 coincides within errors with a ^{13}CO $J=3-2$ peak (Figure 1) and is also apparent in the CS $J=3-2$ map of Fuente *et al.* (1998) as a dense gas condensation. Two of our C^{18}O $J=3-2$ spectra are close to SM 2, i.e. $\sim 5''$ north and south of the sub-mm peak (offsets $(-20''0, 25''0)$ and $(-22''5, 10''0)$). They show slightly elevated excitation temperatures (see Table 2), but the higher kinetic temperature is more likely due to the PDR rim than to any embedded source. The linewidths, especially in C^{18}O , are narrow and there is no evidence for outflow. SM 2 therefore has the appearance of a prestellar core. The virial mass is $\sim 70 M_\odot$, assuming a linewidth of 1 km s^{-1} , i.e. several times larger than the mass we derive from our sub-mm observations. However, it is clear that the hot gas in the cavity has compressed the whole ridge in which SM 2 is embedded. We also note that our derived value for β as well as our assumed dust temperature is rather uncertain and our mass estimate is at most accurate to a factor of two. Therefore we cannot say whether SM 2 is gravitationally stable, if it will disperse or if it will collapse.

4.3. Dust properties

To investigate dust properties across the region, we made a map of the spectral index α ($F_\nu \sim \nu^\alpha$), using the 850 and 450 μm deconvolved images smoothed to $14''$ resolution. Explicitly,

$$\alpha = \log(F_{450}/F_{850}) / \log(850/450) \quad (3)$$

Since at short wavelengths we are likely to chop into the extended dust emission (see Section 3.2), we added a constant level of 5% of the peak value to the flux level in the 450 μm image. This will reduce more the 450 μm than the 850 μm flux, because of the more extended error lobe at 450 μm . The resulting map is shown in Figure 7. The α contour levels range from 3 to 5 in steps of 0.25.

The spectral index map has two striking features. Firstly, a comparison with the 450 μm or 850 μm maps shows a general anticorrelation between submillimeter continuum flux and spectral index. The highest flux positions are minima of α , and the value of α increases towards regions of weaker continuum emission. The α minima are seen at the locations of LkH α 234 SM1, SM2 and the flux peak near the offset $(-45''0, -85''0)$. These continuum peaks are correlated with dense gas clumps, in which opacity is high,

and therefore the spectral index is low. The curving ridge of 450 μm emission (Figure 4) can be followed throughout its length in the α map. A second remarkable feature of the α map is the steep rise in α towards the molecular cavity. This large gradient in α occurs along the entire transition region. The temperature is expected to increase towards the west because of radiation from stars in the cavity.

It is important to determine whether the observed increase in α is due to the change in temperature through the PDR, or in the dust opacity index, β . Because $F_\nu \propto \kappa_\nu^\beta B_\nu(T_d)$, the spectral index, α , and the dust opacity, β , can be related as follows:

$$\alpha = \beta + 2 + \gamma, \quad (4)$$

where γ can be thought of as a correction to the Rayleigh-Jeans form of the Planck function and is given by (Visser *et al.* 1998)

$$\gamma = 1 + \log[(e^{h\nu_{850}/kT} - 1)/(e^{h\nu_{450}/kT} - 1)]/\log(850/450). \quad (5)$$

An increase in α may be due to an increase in the dust temperature, T , and/or in β . The temperature is expected to be higher towards the west because of radiation from stars in the cavity. Our analysis in Section 3.1 showed indeed that a rising gradient of the gas temperature occurs towards the ridge. Is it possible to understand the larger values of α only as due to higher dust temperatures? The answer is no because γ approaches zero at large T so that the maximum value of α is $\beta + 2$. Values of α larger than 4 require $\beta \geq 2$, even if T is large. While the expected increase in T_d toward the cavity will result in higher values of α , the increase in T_d must be accompanied by an increase in β .

Ideally, the above relations can yield the exact value of β , knowing the spectral index α and assuming a temperature for the dust. In practice, the determination of the true value of β is restricted by the current uncertainties in the sub-mm fluxes, especially at short wavelengths, which will reflect into uncertainties in α . The dust will be more optically thick at 450 μm than at 850 μm (since the optical depth changes with frequency as $\tau \sim \nu^\beta$). Thus at 450 μm we do not see deeply into the densest hot cores, while at 850 μm the emission comes from both the hot dust in the core and the surrounding (colder) layer. As mentioned before, we tried to remedy this situation by adding a constant zero-level to the 450 μm flux, but this is only a first order correction. In reality, the dust structure will not be flat, but will have its own substructure, similar to that of the molecular cloud. Also, the numerical values of α in regions of low flux are highly uncertain.

The most important reason for this is the inevitable uncertainty in the flux calibration. When fluxes are low, the flux ratio, which is used in the definition of α , can depart drastically from the "true" value.

In summary, we have confidence in the values of $\alpha \simeq 3$ we find at high flux levels and we believe that the trend of increasing α towards lower flux values is valid, but we do not have confidence in the highest values of α in regions of low flux. In the dense cores we find $\beta < 2$, as suggested by the minima in the spectral index plot as well as our dust fits in Figure 6. Since small grains produce a high β -index and large grains lead to smaller values of β , our results are consistent with the growth of grains in regions of high density.

Our present observations of NGC 7129 support the conclusions of other similar studies that high density clumps or cores have smaller values of β than does the surrounding gas (Visser *et al.* 1998; Johnstone & Bally 1999; Sandell *et al.* 1999). Values of $\beta \sim 2$ outside the flux peaks have been also reported in reflection nebulae surrounding Herbig Ae/Be stars (Whitcomb *et al.* 1981). Our α map goes further, however, in showing a general correspondence between flux and α over an extended area, and in showing a steep increase in α (and, therefore, in β) along an extended PDR.

5. SUMMARY

We have obtained new high resolution maps of the NGC 7129 ridge in submillimeter continuum emission and in ^{13}CO $J=3-2$ line emission. The main results of this study are:

1. A sharp boundary between the molecular ridge and cavity is clearly seen in the ^{13}CO map. A previously detected narrow filament of optical and near infrared emission follows closely the cloud-cavity boundary. Strong emission in the $v=1-0$ $S(1)$ line of H_2 from the filament, if due to fluorescence, supports the interpretation of the boundary as a PDR.
2. The ^{13}CO emission consists of two main "clumps" connected by a bridge of gas. The northern clump has three ^{13}CO peaks, while the southern clump has a single emission maximum.
3. The $850 \mu\text{m}$ and $450 \mu\text{m}$ maps show a very good morphological agreement with the ^{13}CO map. Both data sets show a sharp boundary (cloud rim) toward the cavity where the two young stars BD +65 1637 and BD +65 1638 are located.
4. Three compact sources are seen in the continuum maps (SM 1, SM 2, and FIRS 2 in Table 3). We

have made isothermal dust fits to the measured spectral energy distributions obtained by combining our SCUBA data with earlier observations. The resulting masses, dust temperatures, luminosities and dust emissivities are given in Table 4. We identify SM 1 continuum peak with the deeply embedded infrared source IRS 6 which, according to our fit results, is a young Herbig Be star.

5. For nine positions where we have C^{18}O $J=3-2$ spectra, we use the $^{13}\text{CO}/\text{C}^{18}\text{O}$ intensity ratio to obtain the mass of gas in the $14''$ beam. The masses derived from CO are found to be consistent with masses derived from the dust continuum emission, implying little or no CO depletion in this region.

6. A map of the $850\mu\text{m}/450\mu\text{m}$ spectral index, α , shows a general correlation between the α minima and the submillimeter continuum flux peaks. The low values of α in the peaks also correlate with low values of dust opacity indices, β , in the range 1 to 1.6, suggesting the growth of grains in compact sources. The spectral index α rises steeply towards the molecular cavity, along the entire length of the boundary region. Consequently, the dust opacity index in this region is also high, $\beta \sim 2$. This suggests very hot, small size grains in the PDR ridge, whose mantles have been evaporated by the intense UV radiation.

The James Clerk Maxwell Telescope is operated on a joint basis between the United Kingdom Particle Physics and Astronomy Research Council (PPARC), the Netherlands Organization for the Advancement of Pure Research (ZWO), the Canadian National Research Council (NRC), and the University of Hawaii (UH). The National Radio Astronomy Observatory is a facility of the National Science Foundation operated under cooperative agreement by Associated Universities, Inc. This research was partly supported by an operating grant from the Natural Sciences and Engineering Research Council of Canada.

REFERENCES

Ábrahám, P., Balázs, L. G., Kun, M. 1999, A&A, 354, 645

Bechis, K.P., Harvey, P.M., Campbell, M.F. & Hoffmann, W.F. 1978, ApJ, 2226, 439

Bertoldi, F., Draine, B. T. 1996, ApJ, 458, 222

Bertout, C., Thum, C. 1982, A&A, 107, 368

Bertout, C. 1987, in IAU Symp. 122, Circumstellar Matter, ed I. Appenzeller & C. Jordan (Dordrecht:Reidel), 23

Cabrit, S., Lagage, P.-O., McCaughrean, M. & Olofsson, G. 1977, A&A, 321, 523

Cesarsky, C.J., Cesarsky, D.A., Churchwell, E. & Lequeux, J. 1978, A&A, 68, 33

Clements, E.D., Argyle, R.W. 1984, MNRAS, 209, 1

Di Francesco, Evans II, N. J., Harvey, P. M. 1998, ApJ, 509, 324

Edwards, S., Snell, R.L. 1983, ApJ, 270, 605

Eiroa, C., Palacios, J. & Casali, M.M. 1998, A&A, 335, 243

Emerson, J. P. 1988, in Proc. NATO Advanced Institute, Formation and Evolution of Low Mass Stars, Eds. A. K. Dupré and M. T. V. T. Lago (Dordrecht: Reidel), p 193

Fuente, A., Martín-Pintado, J., Bachiller, R., Neri, R. & Palla, F. 1998, A&A, 334, 253

Giannini, T. *et al.* 1999, A&A, 346, 617

Gibb, A. G., Little, L. T 1998, MNRAS, 295, 299

Goodrich, R.W. 1986, AJ, 92, 885

Güsten, R. & Marcaide, J.M. 1986, A&A, 164, 342

Hartigan, P. & Lada, C. 1985 ApJS, 59, 383

Harvey, P.M., Wilking, B.A. & Joy, M. 1984, ApJ, 278, 156

Henning, Th., Burkert, A., Launhardt, R., Leinert, C. & Stecklum, B. 1998, A&A, 336, 565

Herbig, G. H. and Bell, K. R., 1988, Catalog of emission line stars of the Orion population : 3 : 1988, Lick Observatory Bulletin, Santa Cruz

Hildebrand, R. H. 1983 , Q.Jl R. Astr. Soc., 24, 267

Hodapp, K. W. 1994, ApJS, 94, 615

Holland, W.S., Robson, E.I., Gear, W.K., Cunningham, C., Lightfoot, J.F., Jenness, T., Ivison, R.J., Stevens, J.A., Ade, P.A.R., Griffin, M.J., Duncan, W.D., Murphy, A., Naylor, D.A. 1999, M.N.R.A.S., 303, 659

Hollenbach, D. J. Tielens, A. G. G. M. 1997, AARA, 35, 179

Jenness, T., Scott, P.F. & Padman, R. 1995, MNRAS, 276, 1024

Jenness, T. & Lightfoot, J.F. 1999, Starlink User Note 216.6, Rutherford Appleton Laboratory, Particle Physics & Astronomy Research Council

Johnstone, D. & Bally, J. 1999, ApJ, 510, L49

Lorenzetti, D. *et.al.* 1999, A&A, 346, 604

Miranda, L. F., Eirúa, C., Fernández, M., Gomez de Castro, A. I. 1994 A&A, 281, 864

Mitchell, G. F. & Matthews, H. E. 1994, ApJ, 423, L55

Mitchell, G. F., Johnstone, D., Moriarty-Schieven, G., Fich, M., & Tothill, N. F. H., 2000, submitted to ApJ

Ossenkopf, V. & Henning, T. 1994, A&A, 291, 943

Padman, R 1992, SPECX V6.3 User's Manual (Cambridge: Cavendish Laboratory).

Pollack, J. B., Hollenbach, D. Beckwith, S., Simonelli, D. P., Roush, T. & Fong W. 1994, ApJ, 421, 615

Racine, R. 1968, AJ, 73, 233

Ray, T. P., Poetzel, R., Solf, J. & Mundt, R. 1990 ApJ, 375, L45

Rodríguez, L.F., Moran, J.M., Ho, P.T.P. & Gottlieb, E.W. 1980, *ApJ*, 235, 845

Sandell, G., and Olofsson, H. 1981, *A&A*, 99, 80

Sandell, G. & Weintraub, D., 1994 in *The Nature and Evolutionary Status of Herbig Ae/Be Stars*, ASP conf. Ser. Vol. 62, Eds. P.S. Thé, M.R. Pérez & E.P.J. van Heuvel (Astronomical Society of the Pacific: San Francisco), p. 261 and unpublished draft

Sandell, G. 1997 *Starlink Cookbook 11.1*, Rutherford Appleton Laboratory, Particle Physics & Astronomy Research Council

Sandell, G. *et al.* 1999, *ApJ*, 519, 236

Sandell, G. 2000, *A&A*, 358, 242

Sault, R.J., Teuben, P.J. & Wright, M.C.H. 1995, in *ASP Conf. Ser. 77: Astronomical Data Analysis Software and Systems IV*, Eds. R.A. Shaw, H.E. Payne & J.J.E. Hayes (Astronomical Society of the Pacific: San Francisco), p. 433

Shevchenko, V.S., Yabukov, S.D. 1989, *Sov. Astron.* 33, 370

Skinner, S.L., Brown, A. & Steward, R.T. 1993, *ApJS*, 87, 217

Visser, A. E., Richer, J. S., Chandler C. J. & Padman, R. 1998, *M.N.R.A.S.*, 301, 585

Weintraub, D. A., Sandell, G. 1991, *JCMT-UKIRT Newsletter*, 2, 38

Weintraub, D. A., Kastner, J. H., Mahesh, A. 1994, *ApJ*, 420, L87

Whitcomb, S. E., Gatley, I., Hildebrand, R. H., Keene, J., Sellgren, K. & Werner, M. W. 1981, *ApJ*, 246, 416

Wilking, B.A., Mundy, L.G. & Schwartz, R.D. 1986, *ApJ*, 303, L61

Table 1. Positions of ^{13}CO clumps.

Source	α (2000)	δ (2000)
NGC 7129 ^{13}CO -1	$21^h 43^m 06\rlap{.}^s 7$	$+66^\circ 06' 57\rlap{.}'' 0$
NGC 7129 ^{13}CO -2	$21^h 43^m 03\rlap{.}^s 5$	$+66^\circ 07' 10\rlap{.}'' 0$
NGC 7129 ^{13}CO -3	$21^h 43^m 02\rlap{.}^s 0$	$+66^\circ 07' 28\rlap{.}'' 0$
NGC 7129 ^{13}CO -4	$21^h 42^m 58\rlap{.}^s 5$	$+66^\circ 05' 30\rlap{.}'' 0$

Table 2. Measured properties of the gas.

Offset	$T^* A(^{13}\text{CO})$ (K)	$T^* A(^{18}\text{CO})$ (K)	τ_{13}	T_{exc} (K)	M_{gas} M_\odot
(52''5, 37''5)	3.84	1.32	4.13	13.1	3.6
(-5''0, 13''0)	12.57	4.43	4.27	29.2	7.3
(-20''0, 25''0)	15.73	7.68	6.69	34.7	12.8
(5''0, -8''0)	13.13	3.87	3.35	30.7	11
(0''0, 0''0)	12.8	4.18	3.85	29.8	10.7
(-22''5, 10''0)	14.97	4.96	3.92	33.6	7.2
(-45''0, -85''0)	17.54	5.70	3.82	38.3	8.3
(-30''0, -100''0)	13.04	3.25	2.63	31.5	6.7
(-20''0, -110''0)	7.84	2.97	4.71	20.6	6.4

Table 3. Positions and sizes of compact sub-mm sources.

Source	$\alpha(2000.0)$	$\delta(2000.0)$	$\theta_a \times \theta_b$	P.A. °
LkH α 234 SM1	21 ^h 43 ^m 06. ^s 76	+66° 06' 56".0	6".1 \times 4".9	-46
LkH α 234 SM2	21 ^h 43 ^m 03. ^s 20	+66° 07' 13".1	14".6 \times 9".6	-67
NGC 7129 FIRS 2	21 ^h 43 ^m 01. ^s 51	+66° 03' 24".2	3".9 \times 3".7	n.a.

Table 4. Flux densities, temperatures, total masses and dust luminosities

Source	S_{850} [Jy]	S_{450} [Jy]	T_d [K]	β	M_{tot} M_{\odot}	L_{dust} L_{\odot}
LkH α 234 SM1	3.12	20.7	45	1.24	7.6	8.8×10^3
LkH α 234 SM2	0.73	6.2	30	1.62	4.8	1.4×10^3
NGC 7129 FIRS 2	3.35	18.1	42	1.04	7.0	4.3×10^3

Table 5. Flux densities, assumed dust temperatures, β and total masses.*

Offsets	$S_{850\mu m}$ Jy/14'' beam	$S_{450\mu m}$ Jy/14'' beam	T_d K	β	M_{tot} $M_\odot/14''$ beam
(52''.5, 37''.5)	0.26	1.39 (0.63)	13.1	1.71	6.5
	0.26		13.1	2.0	9.3
(-5''.0, 13''.0)	0.74	6.36 (5.29)	29.2	1.70	5.5
	0.43 ^a		25.0	2.0	8.2
(-20''.0, 25''.0)	0.45	5.18 (3.07)	34.7	2.06	4.1
	0.26 ^a		25.0	2.0	4.6
(5''.0, -8''.0)	1.44	11.6 (10.5)	30.7	1.58	8.6
	0.47 ^a		25.0	2.0	8.5
(0''.0, 0''.0)	3.05	23.1 (22.2)	29.8	1.50	13.9
	0.35 ^a		25	2.0	11.2
(-22''.5, 10''.0)	0.47	4.15 (2.94)	33.6	1.68	2.8
	0.19 ^a		25.0	2.0	4.3
(-45''.0, -85''.0)	0.42	3.33 (2.67)	38.3	1.46	1.6
	0.42		25	2.0	5.9
(-30''.0, -100''.0)	0.19	2.24 (1.08)	31.5	2.14	2.2
	0.19		25.0	2.0	2.5
(-20''.0, -110''.0)	0.13	1.83 (0.75)	20.6	2.67	7.4
	0.13		20.0	2.0	2.3

^aCloud emission only, emission from LkH α 234 SM1 and LkH α 234 SM2 has been subtracted.

Fig. 1.— ^{13}CO $J=3-2$ integrated intensity map superimposed on an K' image of the region (Hodapp, 1994). The squares indicate the nine offsets with complementary C^{18}O $J=3-2$ data which have been chosen for analysis (numbers correspond to the Tabel 1 entries).

Fig. 2.— Composite 850 μm map, including emission from both LkH α 234 and FIRS 2 sources.

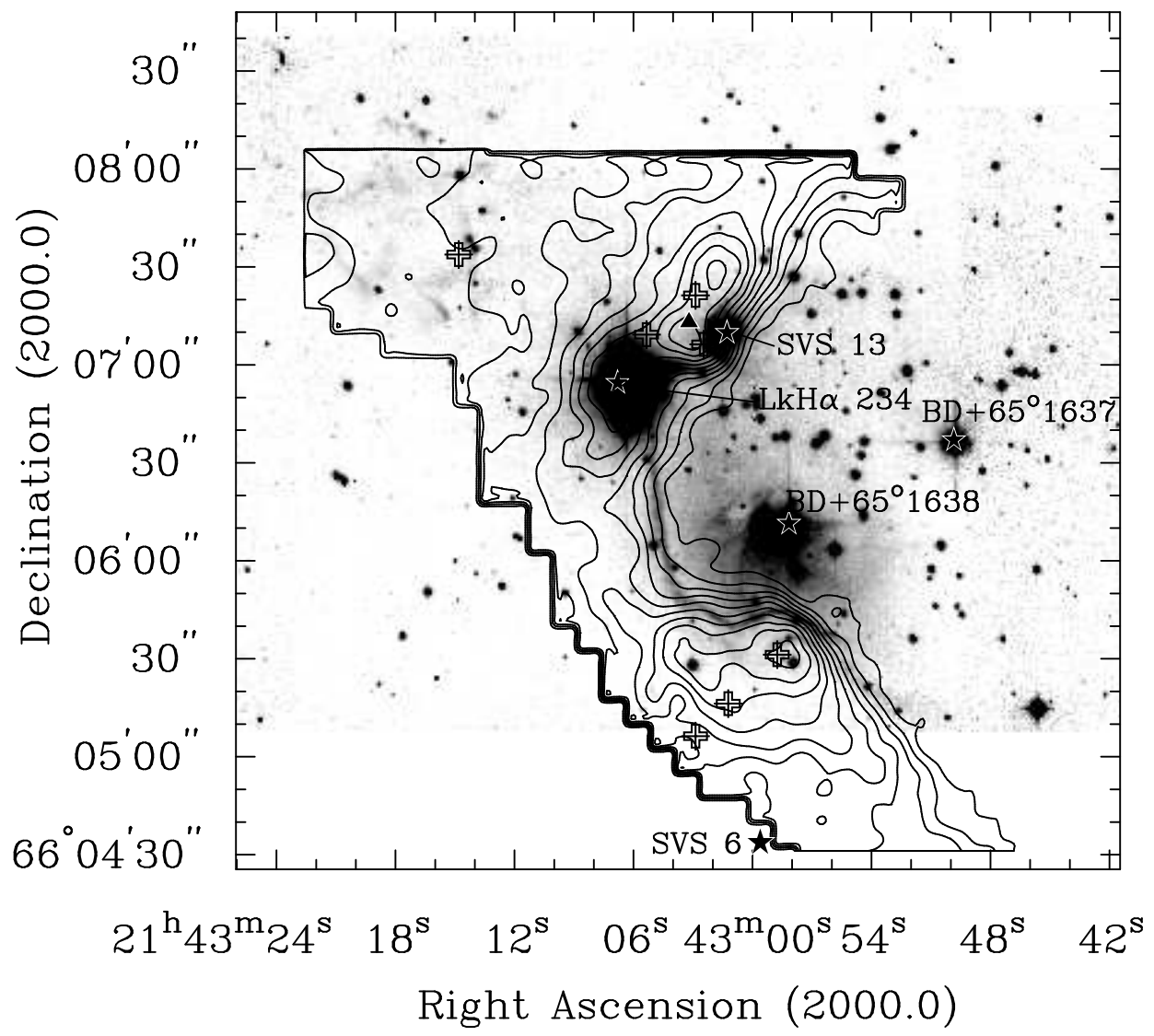
Fig. 3.— The ^{13}CO and C^{18}O $J=3-2$ spectral lines are shown superimposed for the nine chosen offsets. The thin lines correspond to ^{13}CO emission and the thick lines to C^{18}O emission.

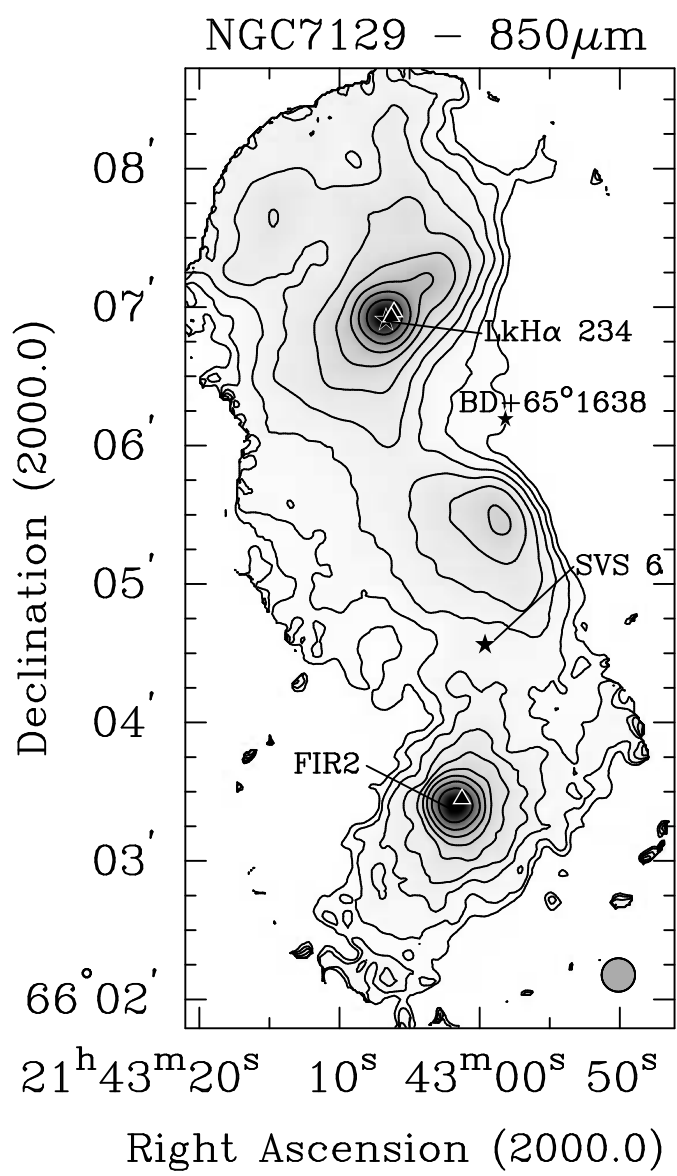
Fig. 4.— Contour map of integrated flux at 450 μm . Contour levels are from 0 to 22.0 Jy/beam in steps of 0.55 Jy/beam for 450 μm .

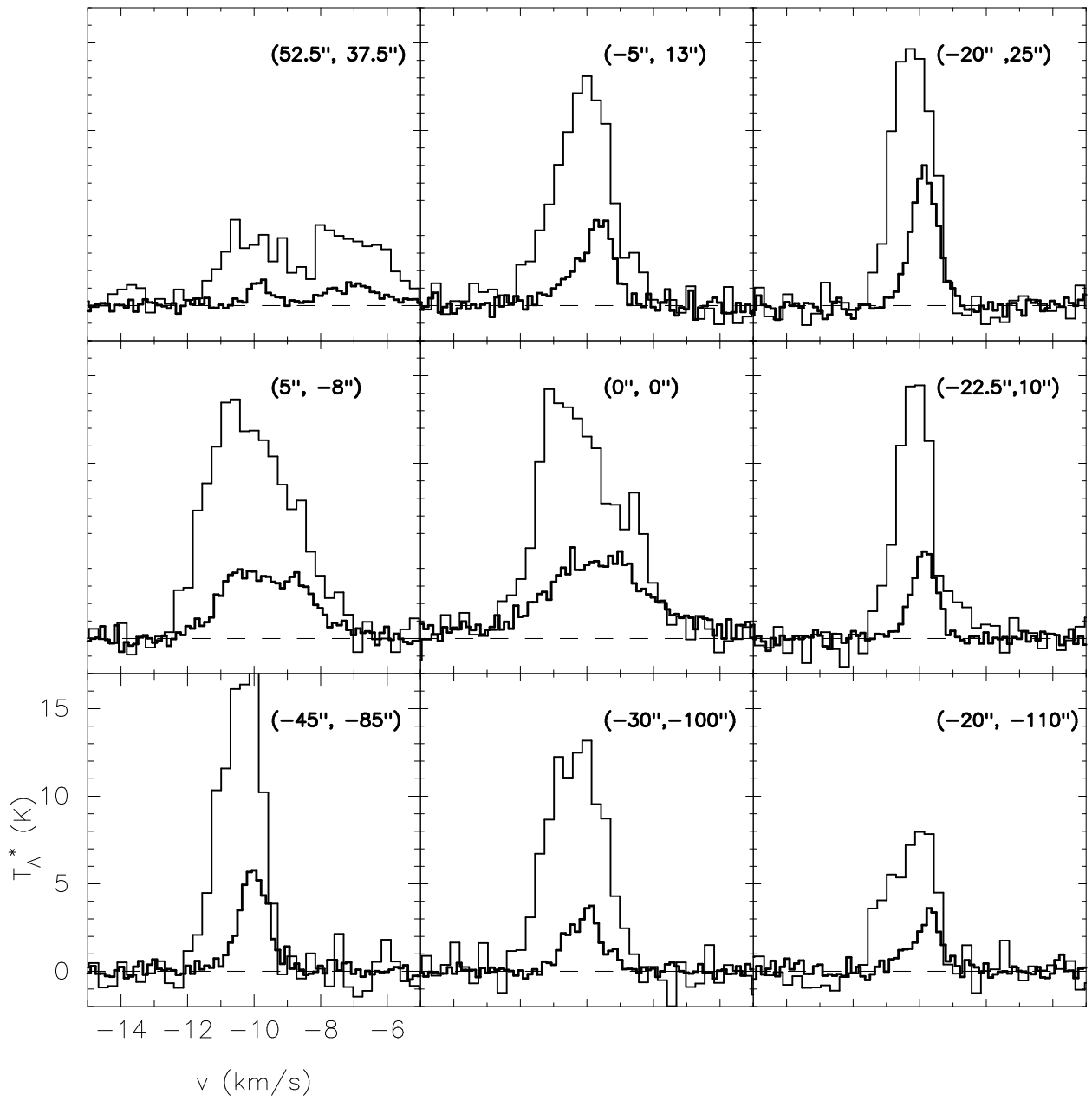
Fig. 5.— Contour map of integrated flux at 850 μm . Contour levels are from 0.1 to 3.0 Jy/beam in steps of 0.096 Jy/beam.

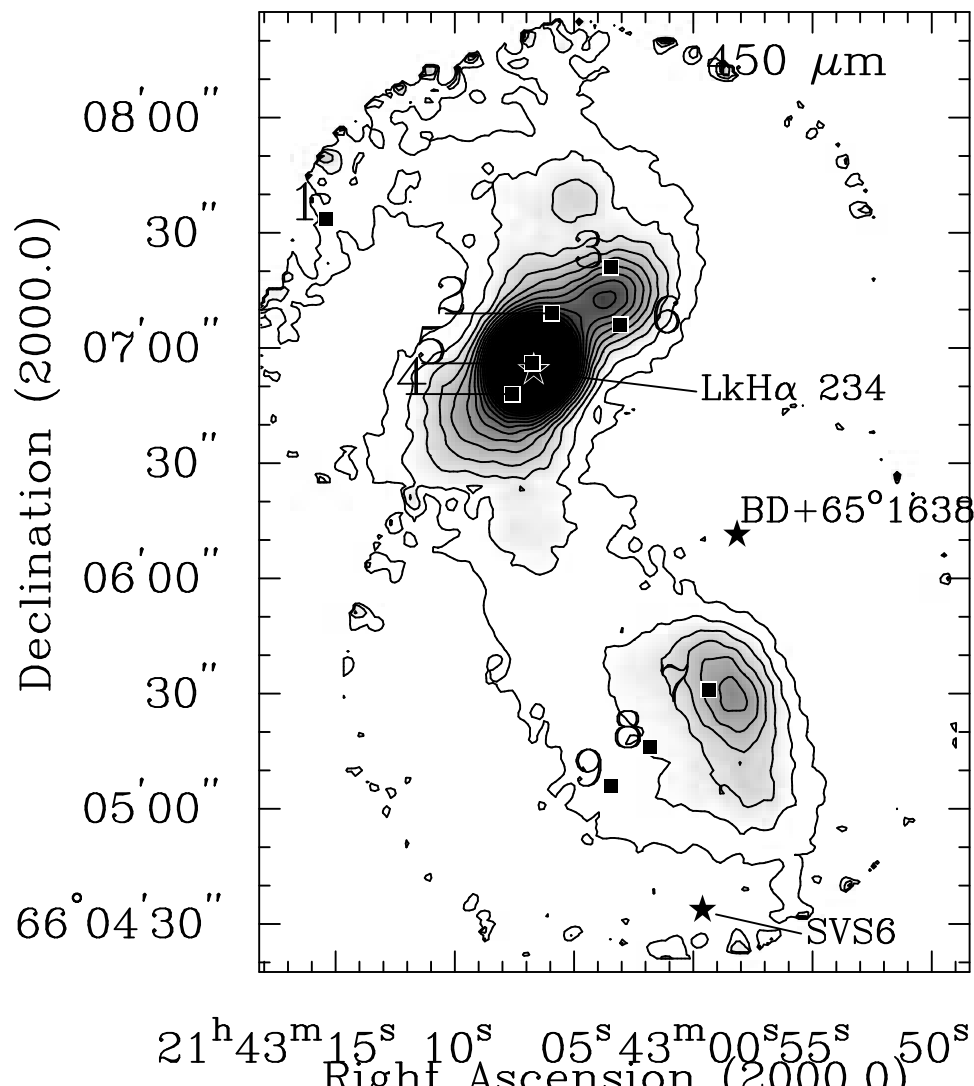
Fig. 6.— Dust fits for LkH α 234 SM1 and NGC7129 FIRS2. The data points include our SCUBA observations, unpublished UKT14 data (Sandell, private communication), as well as IRAS and KAO data (Bechis *et al.* 1978; Harvey, Wilking & Joy 1984). The latter observations were not considered in the fit, because of their large beam sizes that are likely to include hot dust from the surrounding reflection nebulosity.

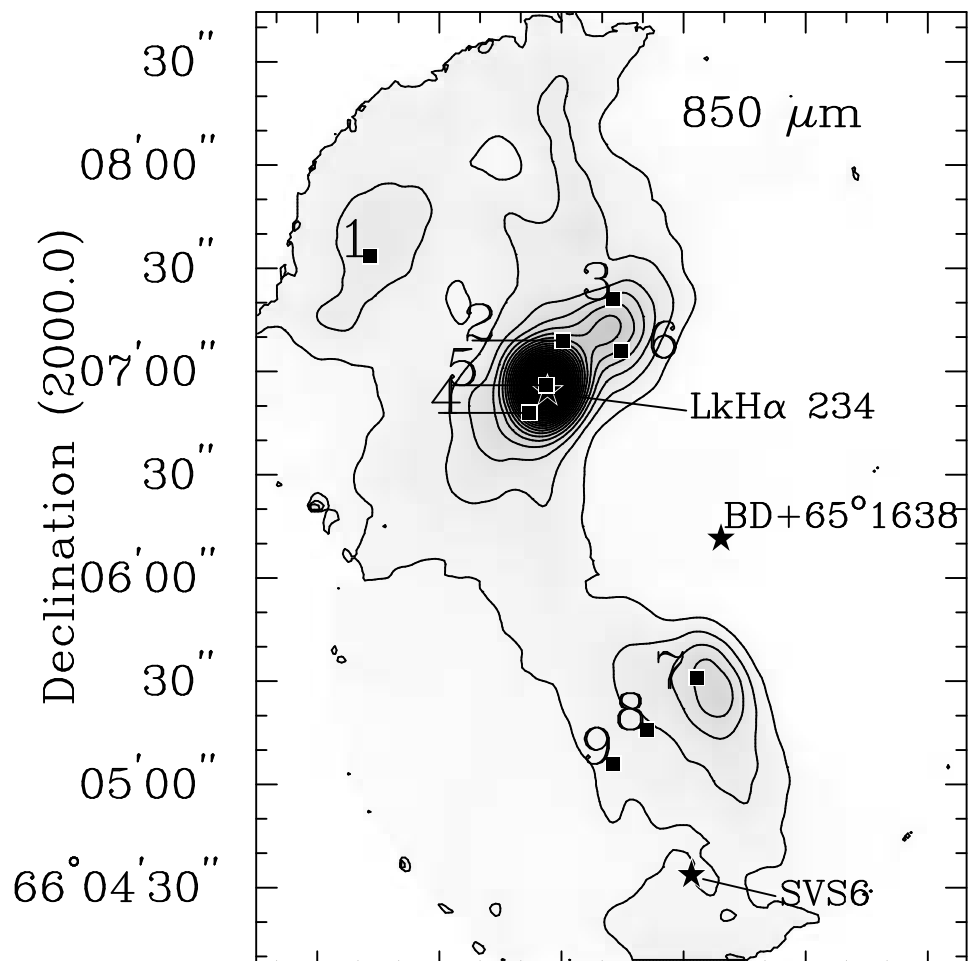
Fig. 7.— Spectral index α map ($F_\nu \sim \nu^\alpha$). Greyscale contours are from 3 to 5, with a step of 0.25. The optical positions were marked with stars and LkH α 234 SM2 source with a rectangle.



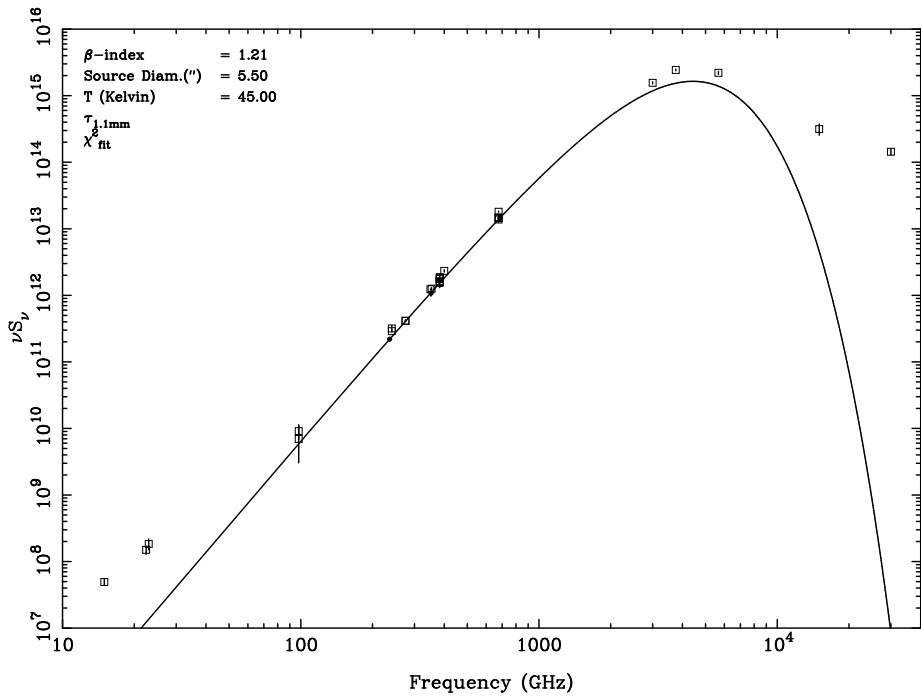








21^h43^m18^s 12^s 06^s43^m00^s54^s 48^s
Right Ascension (2000.0)

LkH α 234 SM1

NGC7129 FIRS2

